ISSN: 2277-3754
ISO 9001:2008 Certified
International Journal of Engineering and Innovative Technology (IJEIT)
Volume 4, Issue 4, October 2014

Synthesis and Electrical Properties of Gamma-Irradiated and Unirradiated Nano-Magnetite

M. Khairy and M.A. Mousa
Chemistry Department, Faculty of Science, Benha University, Benha, Egypt

Abstract*—Nano-sized magnetite (Fe_3O_4) was prepared using dry and wet chemical methods in presence of surfactants as capping agents. The synthesized materials were characterized by X-ray diffraction (XRD), Fourier transform infrared spectroscopy (FT-IR), scanning electron microscopy (SEM) and transmission electron microscopy (TEM). The X-ray diffraction pattern showed cubic spinel crystal structure for all samples. Particle size in the range of 8-55 nm was obtained. The electrical properties (electrical conductivity σ and dielectric constant ε`) of synthesized samples were measured using two-point probe electrical resistivity techniques. Effects of preparation methods and γ- irradiation process on each of the morphology and electrical properties of the prepared samples were studied and discussed. The electrical properties were explained according to electron hopping mechanism between Fe^{2+} and Fe^{3+} ions and found to be dependent on each of particle size and γ- irradiation process.

***Index Terms*—Sol–gel processes, Powders, solid state reaction, Electrical properties, Ferrites.**

I. INTRODUCTION

Magnetic (FeO.Fe2o3) is chemically inert ceramic material with an inverse spinel cubic structure, the oxygen atom forms a closed packing, and the iron cations take up the interstitial tetrahedral or octahedral positions [1]. Magnetite (Fe_3O_4) has attracted an increasing interest in the fields of nanoscience and nanotechnology because of the unique and novel physiochemical properties that can be attained according to their particle size (quantum size effect), shape morphology, and engineering form (films/self-assembled nanocrystals and ferrofluids) [2]. Nano-sized magnetite has been applied in various field of applications such as biomedical [3], absorbent [4], catalysis [5] and passivation coatings [6]. In the last few years [1-12], several synthetic methods and approaches have been applied for preparing nonmaterial. General approaches for shape control and production of anisotropic nanostructures rely on the availability of surfactants, which preferentially absorb on specific crystallographic faces. With ever increasing energy costs, the hydrothermal method could be possibly very attractive for fine powder preparation because of the low temperature involved, crystal size and the morphology of the powders may be controlled by reaction conditions and the good sinter ability of the formed powders [13, 14]. The electrical properties of nanostructure materials, which in most cases precipitously differ from those of their single crystalline, coarse-grained polycrystalline and thin film counterparts is of great theoretical and technological importance. The high surface to volume ratio of the grains, enhanced contribution from the interfacial region, possibility of high defect density are some of the major factors determining the electric response of nanostructure materials[15]. In the present work, we studied the electrical properties of nano-sized magnetite prepared by both wet chemical and thermal dry methods. The materials obtained were characterized by thermal analyses, X-ray diffraction (XRD), Fourier transform infrared (FTIR), scanning electron microscopy (SEM) and transmission electron microscopy (TEM). The effect of γ-irradiation on the structure and electrical properties of our samples was studied.

II. EXPERIMENTAL

A. Materials

Reagent materials such as ferric chloride hexa-hydrate ($FeCl_3 \cdot 6H_2O$, 98%), ferrous chloride tetra-hydrate ($FeCl_2 \cdot 4H_2O$, 99%), ammonium hydroxide (NH_4OH, 28–30% of ammonia), 1-adamantanecarboxylic acid (ACA, 99%), and cetyl pyridinium bromide (CPB) as well as ferrous oxalate dihydrate were purchased from Aldrich and used for magnetite synthesis.

B. Synthesis of magnetite nanoparticles

The magnetite samples were prepared using dry and wetting copreciptation techniques, in absence and presence of ACA and CPB surfactants by methods reported elsewhere[16] .

a) Wet chemical method

Under vigorous and continuous stirring aqueous solution of ferrous and ferric chloride (mole ratio of Fe^{2+}: Fe^{3+} is 1:2) in presence of 10 mmol surfactant was heated at 80-90 ^oC. Concentrated ammonia solution was added slowly into the mixture presents in the reactor. A black precipitate of iron oxides was formed immediately. The ferro-phase was decanted and filtrated to separate the supernatant. The iron oxide powder was washed several times with deionized water. The powder was then heated at 573 K for 5 h. The composition of Fe_3O_4 was verified by $KMnO_4$ titration method [16]. The results showed a ratio of Fe^{3+}:Fe^{2+} agrees with the expected 2:1 ratio within 4%.

b) Dry method

For the dry method, 10 g of ferrous oxalate dihydrate is thermally decomposed, at low oxygen partial pressure, for 6 h at 773 K [12]. The obtained product was then milled in a planetary ball mill. The milling was performed in a closed container with a hardened-steel vial of 120 ml volume and 80 hardened-steel balls of a diameter of 10 mm at ambient temperature. The milling intensity was 200 rpm and the ball-to-powder weight ratio of 20:1 was chosen. The milling process was carried out for two hours. The samples are denoted as S_d for the sample prepared by dry method and as S, S_{CPB} and S_{ACA} for the samples prepared by wetting

ISSN: 2277-3754
ISO 9001:2008 Certified
International Journal of Engineering and Innovative Technology (IJEIT)
Volume 4, Issue 4, October 2014

chemical method without and in presence of CPB and ACA surfactants, respectively. All dry magnetite samples were kept in desiccators on calcium chloride to avoid the oxidation to maghemite. The prepared samples were irradiated by γ-ray source using a ^{60}Co gamma cell (^{60}Co gamma cell 2000 Ci with a dose rate of 1.5 Gy/s (150 rad/s) at a temperature of 30 ^{o}C. Each sample was subjected to a total final dose of 1x10^{5} Gy (10 Mrad). The irradiated samples were distinguished from the unirradiated ones by adding an asterisk beside the symbol of the irradiated samples, e.g. S_d^*.

C. Instrumentation and measurements:

Thermal analysis, XRD, FT-IR, SEM and TEM techniques were employed to characterize structure and morphology of the investigated magnetite samples. The thermal analysis (DTA and TG) was recorded using Schimadzu DT-50 thermal analyzer with samples of about 5 mg in a static air atmosphere and at heating rate 10 K/min. The thermo grams showed thermal stability for all samples over a temperature range of 300 - 773 K. Phase identification of the prepared samples is carried out at room temperature by X-ray diffraction (XRD) patterns using a Philips diffractometer PW 1710 with Cu-Kα irradiation (λ=0.15405 nm). FT-IR spectra were performed by FT-IR spectrophotometer model Perkin-Elmer 599 using KBr pellet technique. The morphologies and microstructures of the as-synthesized samples were observed by JEM-5200 Jeol scanning electron microscope (SEM) and JEOL-2010 transmission electron microscope (TEM), respectively. The electrical measurements were carried out using two point probe method on pellets of 7 mm diameter and thickness ranging between 0.5 and 1mm, prepared by pressing powder under a pressure of 6 x 10^{3} kg /cm^{2} in the temperature range 300–773 K. The electrical parameters were measured using Fluke PM 6306 programmable automatic (RCL) bridge at frequency range of 0 – 10 ^{6} Hz.

III. RESULTS AND DISCUSSION

A. Characterization of the samples

The XRD patterns of the samples prepared are shown in Fig. 1. All samples show characteristic peaks matching well with cubic spinel ferrite Fe_3O_4 (JCPDS file no. 10-0319). The crystallites size D_{XRD}, for the investigated samples were estimated by using Scherrer's equation [17], based on (311) peak:

$$D_{XRD} = 0.9\,\lambda / \beta \cos\theta \quad (1)$$

where λ is the X-ray wavelength, θ the Bragg's angle and β is the pure full width of the diffraction line at half of the maximum intensity. Correction for the line broadening by the instrument was applied using a large particle size silicon standard and the relationship $B^2 = B^2_M - B^2_S$ where B_M and B_S are the measured widths at half-maximum intensity of the lines from the sample and the standard, respectively. The results showed D_{XRD} in the range of 8 – 55 nm, Table 1.

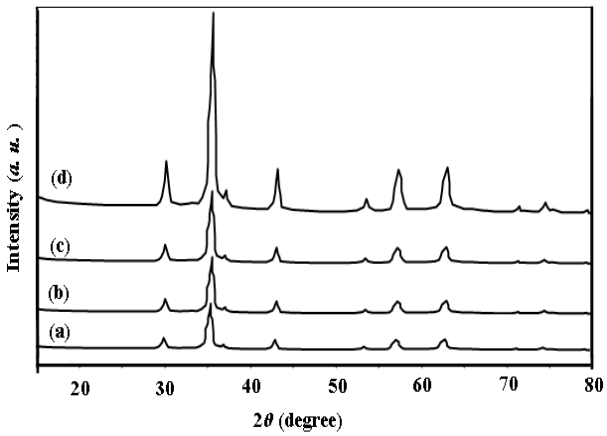

Fig.1: XRD patterns of Fe_3O_4 samples: a)S b) S_d c) S_{CPB} d) S_{ACA}

Table 1. Particle size and FT-IR data of γ-irradiated and unpredicted nano magnetite samples

Samples	Particle size (TEM), nm	Particle size (XRD), nm	υ_o cm^{-1}	υ_t cm^{-1}
S	52	55	384	560
S*	47	51	388	564
S_{CPB}	27(diameter)	38	391	568
S_{CPB}^*	23(diameter)	33	395	571
S_d	19	16	399	571
S_d^*	17	13	401	575
S_{ACA}	9(diameter)	10	405	578
S_{ACA}^*	8(diameter)	8	408	583

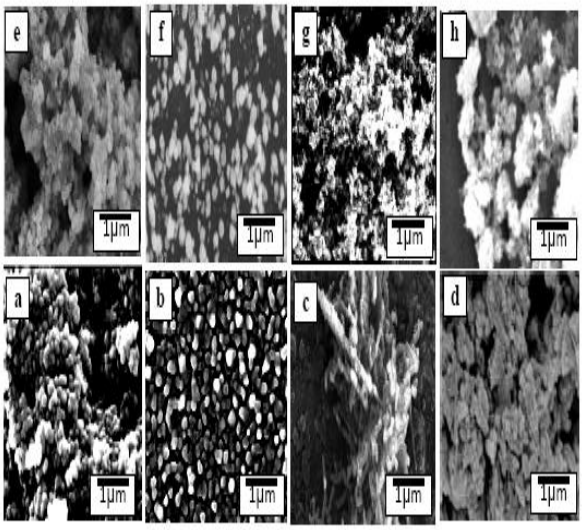

Fig. 2: SEM images of: a)S b) S_d c) S_{CPB} d) S_{ACA} e)S* f) S_d* g) S_{CPB}* h) S_{ACA}*

ISSN: 2277-3754
ISO 9001:2008 Certified
International Journal of Engineering and Innovative Technology (IJEIT)
Volume 4, Issue 4, October 2014

The SEM images of our samples showed surface morphologies depend on the preparation method, Fig.2. This is attributed to that the surfactants may act as a transporter of the particles and as a modifier that leads to the orientation growth of Fe_3O_4 nanoparticle. The SEM image of the sample produced without surfactant showed, on the other hand, a range of shapes including finely dispersed spherical particles with high homogeneity and cotton like structure. There are also different voids between the particles grains. The SEM images of irradiated samples, Fig. 2, showed surface morphologies, which differ slightly than that shown for unirradiated ones. This may be attributed to the creation of some lattice defects by the ionizing radiation. The formation of nanoscale magnetite particles with different morpholgies is confirmed from the TEM images, Fig. 3. The analysis of images obtained reveals that the morphology of the prepared particles depends to a large extent on the type of surfactant used in the preparation method. Where, the micrographs of the sample prepared in absence of surfactant showed large grains with particles do not have a well-defined morphology.

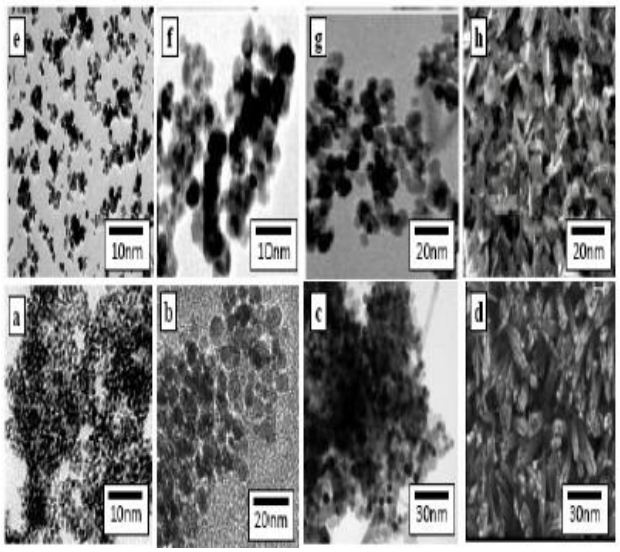

Fig. 3: TEM images of: a)S b) S_d c) S_{CPB} d) S_{ACA} e)S* f) S_d* g) S_{CPB}* h) S_{ACA}*

The TEM images of S and S_d samples show that the Fe_3O_4 particles consist of agglomerated shapes of deformed spheres with an average diameter of 52 and 19 nm, respectively. On the other hand, the samples prepared using surfactants showed the formation of nanorods particles. The TEM images for the samples prepared in presence of surfactants S_{ACA} and S_{CPB} (Figs. 3(c,d,g,h)) show particles with nanorods structure with diameter of 9 nm and length of 0.69 μm as well as 27 nm and length of 3 μm, respectively. These nanorods are a good evidence of ″oriented attachment 'growth, in which the individual particles were aligned like a wall, whereas the second layer of bricks were about to be put on the first. More image analyses showed surface morphologies for the irradiated samples differ slightly than that of unirradiated ones. This indicates that the high ionization radiation produced defects affecting on the surface of the sample. The FTIR spectra for studied samples showed two main vibration bands for the iron-oxygen on both octa- and tetrahedral positions (υ_0) and (υ_t) at 384 - 408 cm^{-1} and at 560-583 cm^{-1}, respectively. This agrees with that found in literature [18]. The peak positions of these vibration modes vary to some extent with particle size, Table 1. A principal effect of the finite size of nanoparticles is producing from the breaking of a large number of bonds for surface atoms, resulting in the rearrangement of localized electrons on the particle surface. As a result, the surface bond force constant increases as Fe_3O_4 is reduced to nanoscale dimension, so that the absorption bands of IR spectra shift to higher wave numbers, as shown in our samples. The FT-IR spectra of irradiated samples showed slight shifts in band positions than that found for unirradiated ones. This may be attributed to the change occurring in the Fe^{2+}/Fe^{3+} ratio as well as the lattice defects producing in the magnetite after irradiation process.

B. DC Conductivity

The temperature dependence of dc-conductivity has been studied for γ-irradiated and unirradiated samples at temperatures ranged between 300 - 773 K. For all samples, the electrical conductivity was found to be a thermally activated process. Typical plots are shown in Fig. 4. All the plots show similar trend, where each curve consists of two straight lines with different slopes. Each one can be expressed by Arrhenius equation:

$$\sigma_{dc} = \sigma_o \exp(E_{dc}/K_bT) \qquad (2)$$

where σ_0 is the pre-exponential factor, E_{dc} is the activation energy and K_b is the Boltzmann constant. From the slopes of the plots the activation energy values, E_{dc}, have been calculated and listed in Table 2. The break in the plots of ln σ_{dc} vs. 1/T at higher temperatures may be attributed to the consolidated of nanoparticles. Inspection of Table 2 shows that the conductivity decreases with the decrease in the particle size. This is because that the nanoparticles introduce grain-boundaries in material and its volume fraction is much more with decreasing the particle size. It had been reported that the grain boundaries in nanocrystalline materials exhibit a random atomic arrangement and producing spatial confinement of free and bound charges [19].

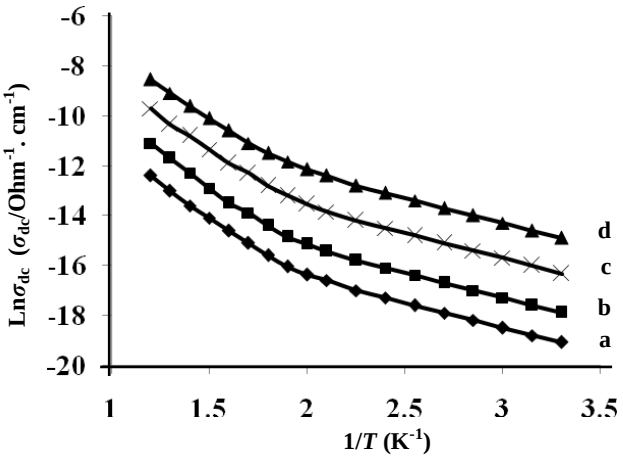

Fig. 4: Effect of temperature on dc-conductivity of Fe_3O_4: a) S_{ACA} b) S_d c) S d) S_{CPB}

ISSN: 2277-3754
ISO 9001:2008 Certified
International Journal of Engineering and Innovative Technology (IJEIT)
Volume 4, Issue 4, October 2014

These results refer to that the volume fraction is very important in determining the electrical properties of consolidated nanoparticles. The electrical conduction in magnetite, $[Fe^{3+}]_t[Fe^{2+}Fe^{3+}]_oO_4^{2-}$, is explained on the basis of an electron exchange between Fe^{2+} and Fe^{3+} ions present on octahedral sites [20]. This is because the distance between two metal ions on octahedral sites (o) is smaller than the distance between two metals ions on (o) and tetrahedral (t) sites; therefore the hopping of electrons between (o) and (t) has very small probability compared with that for o – o hopping. The obtained conductivity data for irradiated samples showed conductivity values less than that of unirradiated ones and activation energies close to that found for uniradiated samples, Table 2. This reveals to that the conduction mechanism is the same in both irradiated and unirradiated samples and the results obtained could be explained by the following mechanism:

$$\gamma + Fe^{2+} \rightarrow Fe^{3+} + e \quad (3)$$

This interaction leads to the creation of Fe^{2+} ions in the tetrahedral sites and at the same time decreases the ratio Fe^{2+}/Fe^{3+} present in the octahedral sites

Sample	D_{XRD} (nm)	Temp. Range (K)	E_a (eV)	σ_{dc} ($ohm^{-1}cm^{-1}$)	σ_b ($ohm^{-1}cm^{-1}$)	ε`
S	55	300-588	0.18	$5.3x10^{-6}$	$6.1x10^{-5}$	4
		588-773	0.43			
S*	51	[300-600]	[0.17]	[$1.2x10^{-6}$]	[$2.4x10^{-6}$]	[7]
		[600-773]	[0.44]			
S_{CPB}	38	300-590	0.18	$1.3x10^{-6}$	$8.2x10^{-7}$	6
		590-773	0.44			
S_{CPB}*	33	[300-610]	[0.18]	[$2x10^{-7}$]	[$5.1x10^{-7}$]	[10]
		[610-773]	[0.43]			
S_d	16	300—625	0.17	$2.6x10^{-7}$	$4.5x10^{-7}$	9
		625-773	0.44			
S_d*	13	[300-610]	[0.18]	[$2.9x10^{-8}$]	[$1x10^{-7}$]	[11]
		[610-773]	[0.43]			
S_{ACA}	10	300-555	0.18	$7.8x10^{-8}$	$3.1x10^{-7}$	14
		555-773	0.44			
S_{ACA}*	8	[300-570]	[0.18]	[$1.1x10^{-8}$]	[$1x10^{-7}$]	[20]
		[570-773]	[0.43]			

*[ ] The irradiated samples

* σ_{dc} dc-conductivity at 500 K, σ_b block conductivity at 500 K and ε`
Dielectric constant at 500 K and in turn decrease the conductivity values [20].

C. AC-Conductivity

The temperature dependence of ac-conductivity $\sigma_{ac}(\omega)$ for the magnetite samples showed the same behavior for each of γ-irradiated and non-irradiated samples, at all testing frequencies; typical plots are shown in Fig. 5. At lower temperatures there is a conductivity variation with frequency, but at higher temperatures all the conductivity curves at different frequencies merge to each other referring to intrinsic conductivity [21]. The influence of temperature on ac-conductivity has been explained by considering the mobility of charge carriers responsible for hopping. As temperature increases the mobility of hopping electrons between $Fe^{2+} \leftrightarrow Fe^{3+}$ ions also increases thereby increasing conductivity.

A common feature of all semiconductor materials is the frequency dependent conductivity, which $\sigma_{ac}(\omega)$ increases with frequency according to [22].

$$\sigma_{ac}(\omega) = \sigma(\omega) - \sigma_{dc} = A\omega^s \quad (4)$$

ISSN: 2277-3754
ISO 9001:2008 Certified
International Journal of Engineering and Innovative Technology (IJEIT)
Volume 4, Issue 4, October 2014

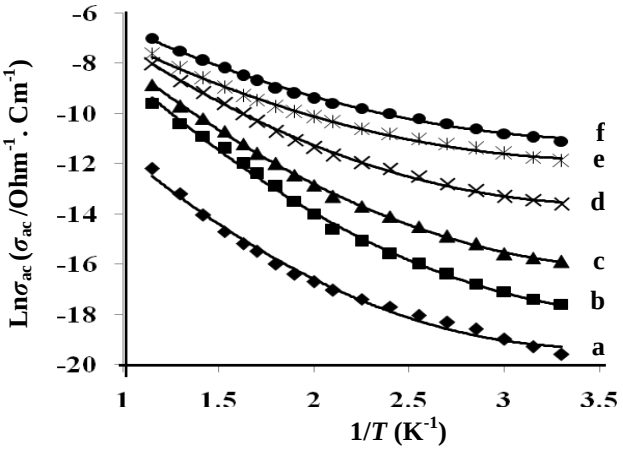

Fig. 5: Effect of temperature and frequency on electrical conductivity of Fe_3O_4: a) 0 Hz b)0.1KHz c)1 kHz d)10 kHz e)100 kHz f)1 MHz

where σ_{dc} is the dc part of the total conductivity $\sigma(\omega)$, A is a constant and $(s \leq 1)$ is the frequency exponent. Our results showed higher σ_{ac} values and lower activation energies than that of σ_{dc} referring to the presence of polarization effect in all investigated samples. For dc-conductivity the charge carriers choose the easiest path between ions, but these paths might include some hops for which the distance between the ions is large. This is not important in ac-conductivity. Thus, lower activation energies may be involved in the ac-conductivity than in dc-conduction [23]. Increasing σ_{ac} with the increase in frequency, Fig. 5, refers to that the hopping mechanism dominates in the samples investigated. This trend was expected because the high frequency acts as pumping force helps the charge carriers to jump between the different localized states. Whereas, at low frequencies the conductivity is low due to grain boundary effect which acts as hindrance for mobility of the charge carriers. The frequency exponent values of s in equation (4) were determined by plotting log σ_{ac} vs log (ω) at different temperatures and was found to lie in the range of 0.05 – 0.58 and decrease with the increase in temperature. This finding suggests that the correlated barrier hopping mechanism is the involved conduction mechanism in all investigated samples [24].

D. Dielectric constant

The effect of temperature on the dielectric constant (ε′) at different frequencies for γ-irradiated and unirradiated magnetite showed the same behavior for all samples. Typical plots are given in Fig 6. It showed that ε′ increases with the increase in the temperature and the decrease in the frequency. This behavior was also Observed by several investigators for various ferrite systems [24, 25]. The mechanism of dielectric polarization is similar to that of conduction, i.e. the electron exchange between $Fe^{2+} \leftrightarrow Fe^{3+}$ at the octahedral sites leading to a local displacement of the electron in the direction of the applied electric field. These displacements determine the polarization of the magnetite. The observed decrease in dielectric constant with increasing frequency is attributed to the fact that the space charge carriers in a dielectric requires a finite time to line up their axes in the direction of an applied alternating field.

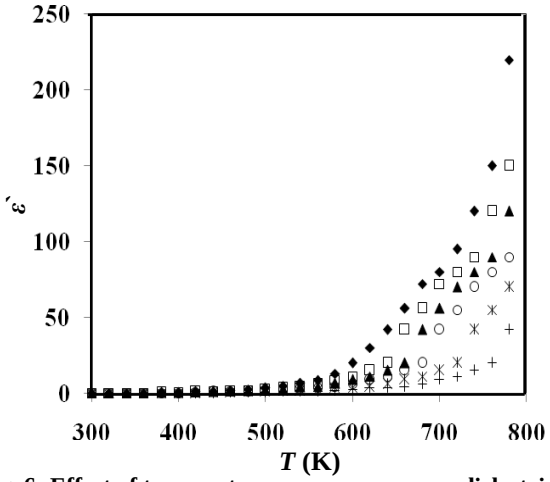

Fig. 6: Effect of temperature and frequency on dielectric constant for nano-magnetite (17 nm): ♦, □, ▲, ○, * and + for 100 Hz, 1 kHz, 10 kHz, 50 Hz, 100 kHz and 1 MHz, respectively.

If the frequency of the field reversal increases, a point reaches when the space charge carriers cannot align with the applied field and does not follow the alternation of the field; as a result dielectric constant of the material decreases. The high values of dielectric constant obtained are attributed mainly to the space charge polarization mechanism, in which the nano-magnetite is assumed to be composed of different structures or regions (grain and grain boundaries). The conductivity of the grain is considered relatively better than the grain boundary. Due to this reason, the charge carriers encounter different resistances so that accumulation of charges at the separating boundaries occurs and hence the dielectric constant value is highly raised. Our results showed an increase in ε ′ values with the decrease in the grain size, Table 2. This is attributed to the increase in the number of grains with decreasing the grain size and also due to large surface polarization owing to the large surface area of individual grains. Increasing ε′ values of irradiated samples compared to those of unirradiated ones might be attributed to the local change occurring in Fe^{2+}/Fe^{3+} ratio or lattice defects produced in the lattice by irradiation process.

E. Complex Impedance Spectroscopy

Complex impedance measurements are routinely used to characterize the dielectric behavior of materials and have proved to be a particularly powerful tool for depicting the electrical conductivity of ionic, electronic, or mixed ceramic materials [26]. The complex impedance z``-z` diagrams for the different specimens showed similar behavior, typical plots are shown in Fig. 7. The plots show semicircles, with centers lie below z` axis. The intersection of z` axis represents the sample bulk resistance R_b at the left end of the circle (at the infinite frequency) stands for the grain resistance, while the right one stands for the whole resistance of the grain and grain boundary [26, 27]. It is clear from Fig. 7 that the diameter of the semicircle

ISSN: 2277-3754
ISO 9001:2008 Certified
International Journal of Engineering and Innovative Technology (IJEIT)
Volume 4, Issue 4, October 2014

decreases with increasing temperature referring to the pronounced decrease in R_b, i.e., increase of dc- conduction. The semicircle diagrams can be interpreted using an equivalent circuit model [27]. In our case, one single semicircular plot, however, might indicate the dominance of one phenomenon. The semicircles are due to a parallel combination of the bulk resistance R_b and the geometric capacitance C_s of the sample. Bulk responses are generally characterized by a low capacitance (in the pF-range) while grain boundaries give rise to larger (nF-range) capacitances [28]. In our samples it is clear that the grain boundaries effect is the dominant phenomenon.

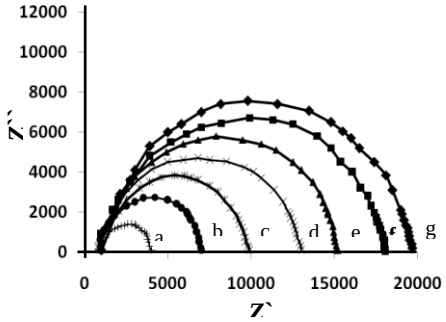

Fig.7: Impedance spectra for nano-magnetite (13 nm) at different temperatures : a) 343 K b)353K c)363K d)373 K e) 383K f) 393 K g) 403 K

IV. CONCLUSION

Nanocrystalline Fe_3O_4 samples were prepared in the range of 8-55 nm. The analysis of XRD patterns reveals spinel cubic structure for the synthesized materials. The particle morphology obtained depends on both the preparation route and the presence of surfactants. Electrical conductivity of the samples increases with increasing the particle size. The conductivity results reveal to the semiconducting nature of all samples. The electrical conduction occurs via electron hopping between Fe^{2+} and Fe^{3+} ions. The electrical conductivity of irradiated samples is found to be lower than that of non-irradiated ones due to a decrease in F^{e2+}/F^{e3+} ratio in octahedral sites after irradiation process. The dielectric constants were found to depend on each of the morphology and the particle size and decreases with increasing the frequency. The complex impedance spectra showed only one semi circle corresponding to the grain boundary resistance.

REFERENCES

[1] X. Liang, Y. Zhong, S. Zhu, H. He, P. Yuan, J. Zhu, Z. Jiang, The valence and site occupancy of substituting metals in magnetite spinel nanostructure $Fe_{3-x}M_xO_4$ (M = Cr, Mn, Co and Ni) and their influence on thermal stability: An XANES and TG-DSC investigation, Solid State Sci., vol. 15, pp115-122, 2013.

[2] T. V. Duncan, Applications of nanotechnology in food packaging and food safety: Barrier materials, antimicrobials and sensors, J. Coll. Inter. Sci., vol.363, no. (1), pp 1-24, 2011.

[3] E. Illés, M. Szekeres, E. Kupcsik, I. Y. Tóth, K. Farkas, A. Jedlovszky-Hajdú, E. Tombácz, PEGylation of surfacted magnetite core–shell nanoparticles for Biomedical application, Coll. Surf. A, vol. 460, pp. 429-440, 2014.

[4] J. G. Parsons, J. Hernandez, C. M. Gonzalez, J.L. Gardea-Torresdey, Sorption of Cr(III) and Cr(VI) to high and low pressure synthetic nano-magnetite (Fe3O4) particles, Chem. Eng. J., vol. 254, pp. 171-180, 2014.

[5] L. Hou, Q. Zhang, F. Jérôme, D. Duprez, H. Zhang, S. Royer, Shape- controlled nanostructured magnetite -type materials as highly efficient Fenton catalysis, Appl. Catal. B: Env., vol. 144, pp. 739-749, 2014.

[6] A. M. Atta, O. E. El-Azabawy, H.S. Ismail, M.A. Hegazy, Novel dispersed magnetite core–shell nanogel polymers as corrosion inhibitors for carbon steel in acidic medium, Corrosion Sci., vol. 53, pp. 1680-1689, 2011.

[7] M. Allarakhia, S. Walsh, Analyzing and organizing nanotechnology development: Application of the institutional analysis development framework to nanotechnology consortia, Technovation , vol. 32, no. (3–4), pp. 216-226, 2012.

[8] Sonalika Vaidya, Amitava Patra, Ashok Kumar Ganguli CdS@TiO2 and ZnS@TiO2 core–shell nanocomposites: synthesis and optical properties, Coll. Surf. A: Physicochem. Eng. Aspects, vol. 363, no. (1–3), pp.130-134, 2010.

[9] V. Mangematin, S. Walsh, The future of Nanotechnologies, Technovation, vol. 32, no. (3–4), pp. 157-161, 2012.

[10] N. Islam, K. Miyazaki, An Empirical Analysis of Nanotechnology Research Domains, Technovation, vol. 30, no. (4), pp. 229-237, 2010.

[11] G. P. Gruère, Implications of nanotechnology growth in food and agriculture in OECD countries, Food Policy, vol.37, no. (2), pp.191-198, 2012.

[12] F. Sanchez, K. Sobolev, Nanotechnology in concrete – a review, Const. Build. Mater. vol. 24, no. (11), pp. 2060-2071, 2010.

[13] C.Y. Haw, F. Mohamed, C.H. Chia, S. Radiman, S. Zakaria, N.M. Huang, H.N. Lim Hydrothermal synthesis of magnetite nanoparticles as MRI contrast agents, Ceram. Inter., vol. 36, pp. 1417-1422, 2010.

[14] K. Byrappa, M. Yoshimura, Hydrothermal Technology for Nanotechnology- A Technology for Processing of Advanced Materials, Handbook of Hydrothermal Technology (2nd Edition), pp. 615-762, 2013.

[15] H. Huili, B. Grindi, G. Viau, L. B. Tahar, Effect of cobalt substitution on the structure, electrical, and magnetic properties of nanorcrystalline Ni0.5Zn0.5Fe2O4 prepared by the polyol process, Ceram. Inter., vol. 40, pp. 16235-16244, 2014.

[16] M. Khairy, Synthesis, Characterization and Magnetic Properties of γ- irradiated and Unirradiated Magnetite Nanopowders, Inter. J. Mater. Chem. vol. 3, no. (5), pp. 106-111, 2013.

[17] H.P. Klug, L.E. Alexander, "X-ray diffraction procedures", Wiley, New York, 1970.

[18] R.D. Waldron, Infrared Spectra of Ferrites, Phys. Review, vol. 99, pp. 1727- 1735, 1955.

[19] M. P. Bondar, Grain-size effect on the properties of materials under dynamic deformation, Combustion, Explosion, and Shock Waves, vol. 44, pp. 365-369, 2008.

ISSN: 2277-3754
ISO 9001:2008 Certified
International Journal of Engineering and Innovative Technology (IJEIT)
Volume 4, Issue 4, October 2014

[20] P.P. Naik, R.B. Tangsali, S.S. Meena, Pramod Bhatt, B. Sonaye, S. Sugur,Gamma radiation roused lattice contraction effects investigated by Mössbauer spectroscopy in nanoparticle Mn–Zn ferrite, Rad. Phys. Chem., vol. 102, pp.147-152, 2014.

[21] N. Parasad, G. Prasad, M. Kumar, S. Suryanaryana, T. Bhimasankaram, and G. Kumar, Effect of HIPing on conductivity and impedance measurements of DyBi5Fe2Ti3O18 ceramics, Bull. Mater. Sci, vol. 23, pp. 483-489, 2000.

[22] E. Huseynov, A. Garibov, R. Mehdiyeva, Temperature and frequency dependence of electric conductivity in nano-grained SiO2 exposed to neutron irradiation, Physica B: Condensed Matter, vol. 450, pp. 77-83, 2014.

[23] S. Mazen and H. Dawoud, Temperature and composition dependence of dielectric properties in Li–Cu ferrite, Mater. Chem. Phys., vol. 82, pp. 557- 566, 2003.

[24] M. Mohammed, Kh. Abd-Allah and M. Hassan, The Conduction Mechanism and Dielectric Behavior of Sodium Borate Glasses Containing Fe and Bi ions, Egypt. J. Solids, vol. 27, pp. 299-308, 2004.

[25] D. Ravinder and A. Reddy, Dielectric properties of Li–Ge ferrites, Mater. Lett., vol. 57, pp. 2855-2860, 2003.

[26] E. Barsoukov and J. Macdonalds, Impedance Spectroscopy Theory, Experiment and Applications", John Willey & Sons, Inc., 2nd Edition, 2005.

[27] H. Zaki, AC conductivity and frequency dependence of the dielectric properties for copper doped magnetite, Physical B: Condensed Matter, vol. 363, pp. 232-244, 2005.

[28] A. Sellai and H. Widatallah, Some electrical characteristics of Li0.5CrxFe2.25−xO4 spinel structures, Ceram. Inter., vol. 30, pp. 1347-1352, 2004.